Research Letter

How to Cite: *J. Inorg. Mater.*, 2026, **41(4):** 527
DOI: 10.15541/jim20250165

Fe Doped Ti-MOFs for Enhanced Antibacterial Sonodynamic Therapy of Periodontitis

WANG Haoyu[1,2], KE Xue[1,2], GUAN Shiwei[1,2], QIAN Shi[1,2], LIU Xuanyong[1,2]

(1. State Key Laboratory of High Performance Ceramics, Shanghai Institute of Ceramics, Chinese Academy of Sciences, Shanghai 200050, China; 2. Center of Materials Science and Optoelectronics Engineering, University of Chinese Academy of Sciences, Beijing 100049, China)

Abstract: Periodontitis is a clinical challenge caused by bacterial overgrowth, resulting in irreversible damage to periodontal tissue. Antibacterial sonodynamic therapy (aSDT) has emerged as a promising alternative to conventional debridement due to its excellent biocompatibility and tissue penetration capability. However, this therapy cannot cure the periodontitis solely, needing more exploration to find an effectively improved treatment. Here, Fe doped Ti based metal-organic frameworks (Fe/Ti-MOFs) were prepared to explore the relationship between Fe doping and sonoresponsive efficiency. Incorporation of Fe enabled precise modulation of the band structure and crystallinity while maintaining the lattice architecture. Results showed that Fe/Ti-MOFs exhibited enhanced hydroxyl radical (•OH) generation under ultrasonic irradiation, effectively facilitating the eradication of bacterial pathogens. Notably, the sample with a Fe/Ti molar ratio of 0.025 : 1 exhibited exceptional performance. The sonocatalytic activity was collectively influenced by bandgap engineering, Fe doping concentration and crystallinity. Moreover, Fe/Ti-MOFs exhibited no cytotoxicity toward gingival fibroblasts and maintained excellent biocompatibility, without adverse effects on tissue repair. The ultrasound responsive Fe/Ti-MOFs material developed in this study offers potential for mitigating the adverse effects of antibiotics and providing novel insights and strategies for the application of aSDT in periodontitis treatment.

Key words: antibacterial; sonodynamic therapy; periodontitis; metal organic framework; NH_2-MIL-125(Ti)

Periodontitis is one of the most prevalent oral diseases, primarily caused by the excessive proliferation of pathogenic bacteria (*e.g.*, *Porphyromonas gingivalis*) in the oral cavity. The bacterial overgrowth disrupts balance of the oral microbiota and induces inflammation in the periodontal tissue[1]. Proliferation of pathogenic bacteria leads to progressive deterioration of periodontal tissue, characterized by periodontal pocket formation with purulent exudation, tooth loosening, and eventual tooth loss. Furthermore, periodontitis can cause systemic diseases such as osteomyelitis and atrial fibrosis[2], seriously impacting patient health. Currently, the clinical management of periodontitis mainly involves surgical mechanical debridement combined with antibiotics or other antibacterial agents. However, surgical interventions often suffer from incomplete debridement and potential damage to surrounding healthy tissues. Additionally, prolonged antibiotics use poses risks of bacterial resistance, resulting in suboptimal clinical outcomes[3-4]. Therefore, the development of novel, controllable and effective bacterial clearance methods holds promise for improving treatment of periodontitis.

In recent years, antibacterial sonodynamic therapy (aSDT) has shown considerable promise in the field of non-invasive therapy[5-7]. By utilizing low-intensity ultrasound to activate the sonosensitizer, aSDT can enhance the generation of reactive oxygen species (ROS), thereby effectively eradicating bacterial pathogens. This method is highly controllable and reduces the risk of bacterial resistance development. Traditional organic and inorganic sonosensitizers face potential phototoxicity and difficulty in degradation, respectively[8-9]. Application of metal-organic frameworks (MOFs) as sonosensitizers represents a viable and promising approach[10]. NH_2-

Received date: 2025-04-19; **Revised date:** 2025-05-11; **Published online:** 2025-06-05
Foundation item: National Natural Science Foundation of China (52450110)
Biography: WANG Haoyu (2000–), male, Master candidate. E-mail: wanghaoyu222@mails.ucas.ac.cn
王浩宇(2000–), 男, 硕士研究生. E-mail: wanghaoyu222@mails.ucas.ac.cn
Corresponding author: QIAN Shi, professor. E-mail: qianshi@mail.sic.ac.cn
钱 仕, 研究员. E-mail: qianshi@mail.sic.ac.cn

MIL-125(Ti), a titanium-based MOFs with 2-aminoterephthalic acid as the ligand, exhibits a large specific surface area and a distinctive pore structure[11-13]. Additionally, biological safety of its biodegradation products has been validated, offering significant advantages for biomedical applications[14]. NH_2-MIL-125(Ti) has been extensively studied as a sonosensitizer. Liang *et al*.[15] introduced oxygen vacancy defects into NH_2-MIL-125(Ti), substantially enhancing its ROS production under ultrasound irradiation. Wang *et al*.[16] doped NH_2-MIL-125(Ti) with Mn as a heteroatom, significantly improving its ultrasonic responsiveness. However, surface oxygen vacancies have been prone to repair during the reaction process[17]. Moreover, relationship between the doping concentration of heteroatoms and ultrasound response efficiency remains unclear. Furthermore, the therapeutic effect of titanium-based MOFs against bacterial infections requires further investigation.

Given that Fe atoms can coordinate with 2-aminoterephthalic acid to form MOFs, and the secondary building unit consists of FeO hexahedrons with a structure similar to that of NH_2-MIL-125(Ti)[18-19], doping NH_2-MIL-125(Ti) with Fe as a heteroatom is anticipated to minimize potential adverse effects such as lattice distortion. This approach facilitates investigation of relationship between Fe doping concentration and ultrasonic response efficiency. Therefore, the Fe doped NH_2-MIL-125(Ti) was synthesized, and its structural characteristics and sonoresponsive efficiency were systematically studied. Moreover, Fe has been shown to inhibit secretion of heme carrier protein by *Porphyromonas gingivalis*, which is expected to suppress its proliferation during periodontitis treatment[20-21]. Additionally, the antibacterial performance and biocompatibility were also evaluated.

1 Experimental

1.1 Preparation of Fe/Ti-MOFs

Fe/Ti-MOFs samples were synthesized using acetylacetonate iron ($Fe(acac)_3$, Adamas) and tetraisopropyl titanate (TTIP, Adamas) in the molar ratios of 0, 0.025 : 1, 0.05 : 1, and 0.1 : 1, corresponding to the respective sample names as displayed in Table S1 with specific reagent dosages. *N*,*N*-dimethylformamide (DMF, Adamas) and methanol (CH_3OH, Lingfeng) were added to a beaker, followed by addition of 2-aminophthalic acid (H_2BDC-NH_2, Aladdin), TTIP, and $Fe(acac)_3$. The mixture was stirred for 20 min, then transferred to a polytetrafluoroethylene-lined hydrothermal reactor and maintained at 150 ℃ for 36 h. Subsequently, the solid products were collected *via* centrifugation, washed with DMF and methanol until colorless supernatants were obtained, and dried under vacuum at 60 ℃ for 12 h. Finally, Ti-MOFs and Fe/Ti-MOFs powders were obtained through grinding.

1.2 Characterizations and ultrasonic responsiveness

Surface topographies of samples were characterized using a scanning electron microscope (SEM, S-3400N, Hitachi, Japan). The chemical compositions and phases were analyzed by Fourier transform infrared spectrometer (FT-IR, Equinox 55, Bruker, Germany), X-ray diffractometer (XRD, D2 Phaser, Bruker, Germany) and X-ray photoelectron spectroscopy (XPS, K-Alpha, Thermo Fisher Scientific, USA). The UV-Vis full scattering spectrum was measured with a UV spectrophotometer (Lambda 750, PerkinElmer, USA). The photocurrent response (UV-I) of the samples was evaluated using an electrochemical workstation (Autolab PGSTAT 302N, Wetrohm, Switzerland). The specific surface area and pore structure were characterized by a specific surface area and pore size analyzer (Autosorb-iQ, Quantachrome, USA).

Dispersion solutions (2.0 mg/mL) for each group of samples were prepared using ultrapure water. After soaking for 0, 1, 3 and 5 days, the extraction solutions were obtained after centrifugation. The maximum fluorescence intensity of the extraction solutions was measured in a range of 400–500 nm under light excitation at 340 nm.

Methylene blue (MB) was employed as an indicator to evaluate the ability of MOFs to catalyze the generation of •OH under ultrasound (US+) and non-ultrasound (US–) conditions (1 MHz, 1.5 W/cm^2, 50% duty cycle). MOFs solutions (1 mL, 0.2 mg/mL) were mixed with MB solutions (1 mL, 40 μg/mL). Subsequently, the US+ and US– groups were incubated in a dark environment for 10 min. The absorbance changes within the range of 500–800 nm before and after reaction were measured using an enzyme-linked immunosorbent assay (ELISA, Cytoson 5, Biotek, USA). Meanwhile, MOFs solutions (490 μL, 0.1 mg/mL) were mixed with 10 μL of 5,5-dimethyl-1-pyrroline-*N*-oxide (DMPO) and transferred to an X-band desktop continuous wave electron paramagnetic resonance spectrometer (ESR, EMXnano, Bruker, Germany) under US+ treatment for 2 min.

1.3 Antibacterial activity

Staphylococcus aureus (*S. aureus*), *Escherichia coli* (*E. coli*) and *Porphyromonas gingivalis* (*P. gingivalis*) were selected as model bacteria to evaluate the antibacterial performance of samples under US+ and US– conditions. In a centrifuge tube, 500 μL of sample dispersion (2.0 mg/mL in physiological saline) was mixed with 500 μL of bacterial suspension (1×10^6 CFUs/mL), and the mixture was thoroughly shaken. For the ultrasound

group, the solutions were exposed to ultrasound for 10 min (1 MHz, 1.5 W/cm^2, 50% duty cycle). After processing, the solutions from each group were serially diluted, dropped and spread onto agar culture plates, and then incubated at 37 ℃. *P. gingivalis* was cultured in an anaerobic workstation (AW200SG, Electrotek, Britain).

After cultivation, the culture plates were photographed, and the colony-forming units (CFUs) were quantified by counting. The antibacterial rates of the samples were calculated using formula (1):

$$\text{Antibacterial rate} = \frac{N_0 - N_x}{N_0} \times 100\% \quad (1)$$

where, N_0 and N_x denote the number of CFUs in the control and experimental groups, respectively.

1.4 Biocompatibility

Human gingival fibroblasts (HGFs) were cultured in fibroblast medium (FM) medium supplemented with 2% fetal bovine serum (FBS), 1% fibroblast growth supplement (FGS), and 1% penicillin-streptomycin (P/S). Cells were maintained and passaged in an incubator set at 37 ℃ with 5% CO_2.

MOFs solutions (1.0 mg/mL) were prepared for each group in FM culture medium and incubated at 4 ℃ for 24 h. Then, the solutions were filtered using a sterile 0.2 μm filtration device to obtain extraction solutions. HGFs were seeded into a 24-well plate at a density of 1×10^4 cells per well and cultured for 24 h. The original culture medium was then replaced with 1 mL of extraction solution per well. Cells were cultured for an additional 5 days with the medium refreshed every 24 h. After cultivation, the wells were washed with basic FM medium. The cells were stained with Calcein AM/PI at 37 ℃ for 30 min and subsequently observed and photographed under a fluorescence microscope (IX83, Olympus, Japan).

The cytotoxicity of MOFs extraction solutions was evaluated using the Alamar Blue fluorescence assay. HGFs were seeded into a 24-well plate at a density of 1×10^4 cells per well and cultured for 24 h. The original culture medium was replaced with 1 mL of extraction solution per well. Cells were cultured for 1, 3, and 5 d, with the medium refreshed every 24 h. After cultivation, the extraction solution was removed, and 500 μL of basic FM medium containing 10% Alamar Blue reagent was added and incubated for 2 h. Fluorescence intensity was subsequently measured at wavelengths of 560 nm (excitation) and 590 nm (emission) using an ELISA reader.

The blood compatibility of MOFs was assessed using coculture and extraction methods. Fresh defibrated sheep blood was diluted with physiological saline at a volume ratio of 4 : 5, with physiological saline serving as the negative control group and ultrapure water as the positive control group. Physiological saline dispersions of MOFs samples (1.0 mg/mL) were prepared, shaken for 24 h, and centrifuged to obtain physiological saline extracts. Subsequently, 800 μL of each dispersion or extraction solution was mixed with 40 μL of diluted blood and incubated at 37 ℃ for 1 h. After incubation, the mixture was centrifuged at 1000 r/min for 10 min, and the supernatant was collected. Absorbance of the supernatant was measured at 545 nm using ELISA, and the hemolysis rate was calculated according to formula (2):

$$\text{Hemolysis rate} = \frac{\text{OD}_{\text{sample}} - \text{OD}_{\text{NaCl}}}{\text{OD}_{\text{UPW}} - \text{OD}_{\text{NaCl}}} \times 100\% \quad (2)$$

where, $\text{OD}_{\text{sample}}$, OD_{NaCl}, and OD_{UPW} denote the absorbance of the experimental group, negative control group, and positive control group, respectively.

The mean±standard deviation (SD) was recorded using OriginPro 2021 software. All data used for statistical analysis must be repeated three times or more. Data were analyzed *via* one-way analysis of variance (ANOVA) followed by Tukey's post hoc test. Statistical significance was defined as *p<0.05, **p<0.01, and ***p<0.001.

2 Results and discussion

SEM images of MOFs with different Fe doping levels are presented in Figs. 1(a1-a4). Ti-MOFs exhibited a round cake-like structure with diameters ranging from approximately 600 nm to 1000 nm. As the Fe doping amount increases, the sample thickness decreased from approximately 270 nm to 31 nm. XRD results are shown in Fig. 1(b), displaying prominent diffraction peaks at approximately 2θ=6.77°, 9.43°, 9.70°, and 11.62°, which are consistent with the standard NH_2-MIL-125(Ti) diffraction peaks corresponding to the (101), (100), (001), and (211) crystal planes, respectively. This indicated that the Fe doping did not alter the original lattice structure. Furthermore, as the Fe doping level increased, the intensity of the diffraction peaks in the Fe/Ti-MOFs pattern decreased, and the full width at half maximum (FWHM) of the diffraction peaks gradually increased (Table S2), suggesting that the crystallinity of the samples gradually decreased with increasing Fe doping level.

FT-IR spectra (Fig. 1(c)) revealed vibration peaks corresponding to characteristic functional groups such as primary amine (–NH_2) and carboxyl group (–COO) of H_2BDC-NH_2 in all groups. Notably, vibrations associated with metal-oxygen bonding (Fe/Ti–O) were observed in the range of 400–600 cm^{-1}, indicating the successful incorporation of Fe atoms into the lattice structure.

The secondary building unit of NH_2-MIL-125(Ti) is the Ti–O octahedral ring located on the (001) crystal

plane[11-12]. Upon incorporation of Fe atoms, substitutions resulted in a shift of the originally overlapping positive and negative charge centers, thereby increasing the overall negative charge density and destabilizing the system (Fig. S1). As the Fe doping level further increased, the proportion of Fe atoms in the Fe/Ti–O octahedral ring rose synchronously. The increased polarity disrupted the lattice structure of the sample, leading to a reduction in crystallinity.

Brunauer-Emmett-Teller (BET) testing was conducted to characterize the specific surface area and pore structure of the samples. From the N_2 adsorption-desorption isotherms (Fig. 1(d)), it can be observed that the samples exhibit the type I adsorption isotherm characteristic typical of microporous materials. Although the specific surface area showed a trend of first increasing and then decreasing with the increase in Fe doping levels, the overall change remains insignificant (Table S3). Additionally, pore structure analysis revealed that all samples possessed similar structures.

XPS results (Fig. 2 and Fig. S2) indicated that characteristic peaks of C1s (284.8 eV), N1s (399.4 eV), Ti2p (458.8 eV), and O1s (531.8 eV) were detected in Ti-MOFs samples. In Fe/Ti-MOFs, characteristic peaks of C1s, N1s, Ti2p, O1s, and Fe2p (710.8 eV) were observed. The intensity of Fe2p peak increased with increasing Fe doping levels. The high- resolution XPS spectra of Ti2p revealed peaks at binding energies of 458.8 and 464.6 eV, corresponding to the tetravalent $Ti2p_{3/2}$ and $Ti2p_{1/2}$ peaks, respectively. It was confirmed that the titanium atoms in the TiO cluster maintained a tetravalent oxidation state (IV), indicating that the Fe atoms did not alter the chemical environment of Ti atoms. The high-resolution Fe2p XPS spectra showed that peaks at 711.7 and 725.3 eV were attributed to $Fe^{3+}2p_{3/2}$ and $Fe^{3+}2p_{1/2}$, respectively, while peaks at 709.8 and 723.4 eV were assigned to $Fe^{2+}2p_{3/2}$ and $Fe^{2+}2p_{1/2}$. Satellite peaks associated with $Fe2p_{3/2}$ were also detected.

Results of light absorption are presented in Fig. 3(a). For Ti-MOFs, boundary of the light absorption range is determined by the ligand 2-aminoterephthalic acid and TiO clusters. With increasing Fe doping levels, the boundary of the light absorption range for Fe/Ti-MOFs extended into the visible light region, primarily due to the formation of FeO clusters induced by Fe doping, indicating that the Fe incorporation enhanced the light harvesting capability of the samples. Using the Tauc plot analysis method, the UV-visible diffuse reflectance spectrum is converted into a graph depicting the relationship between the absorption coefficient (αhv) and photon energy (hv) based on the formula $(\alpha hv)^2=K(hv-E_g)$, where K is a constant. By extrapolating the linear portion of the curve shown in the Fig. 3(b) in dotted line to the horizontal axis, the intercept corresponding to the intersection point represents the semiconductor bandgap width (E_g). As the doping concentration of Fe increased, the bandgap width gradually decreased: Ti-MOFs at 2.70 eV, Fe/Ti-MOFs (0.025 : 1) at 2.57 eV, Fe/Ti-MOFs (0.05 : 1) at 2.54 eV, and Fe/Ti-MOFs (0.1 : 1) at 2.51 eV. This reduction in bandgap is anticipated to enhance sensitivity to external field stimulation.

From the qualitative and quantitative analysis of Fig. S3, it can be concluded that the Ti-MOFs and Fe/Ti-MOFs have a certain degree of degradability, and its

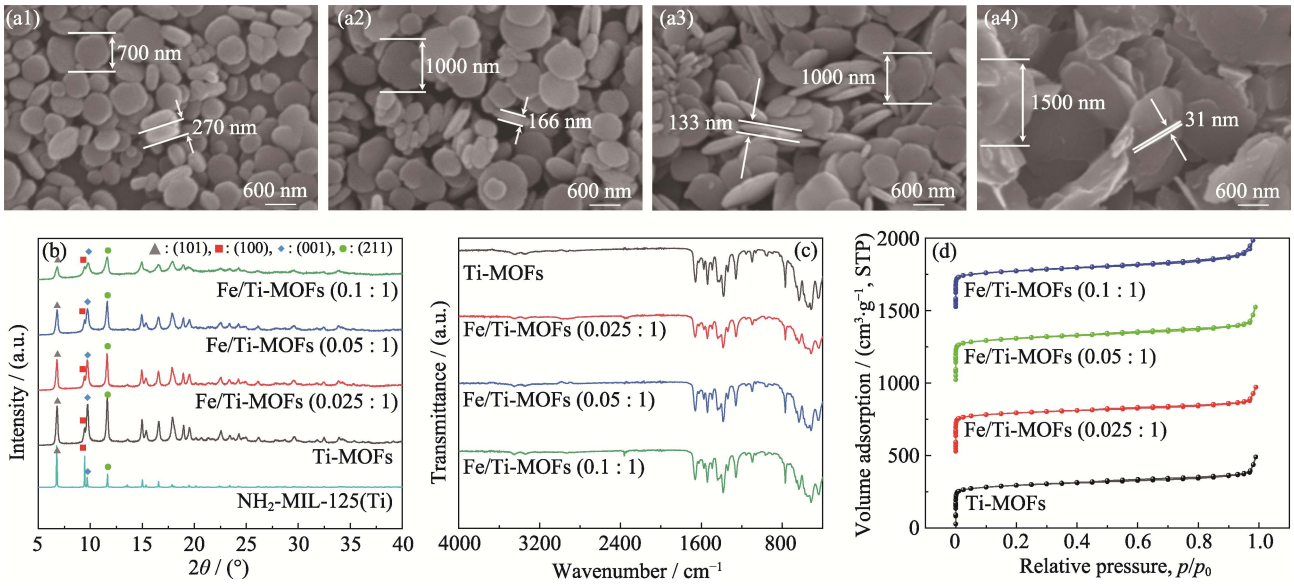

Fig. 1 SEM images of Ti-MOFs (a1), Fe/Ti-MOFs (0.025 : 1) (a2), Fe/Ti-MOFs (0.05 : 1) (a3), and Fe/Ti-MOFs (0.1 : 1) (a4); XRD patterns (b), FT-IR spectra (c), and N_2 adsorption desorption curves (d) of samples

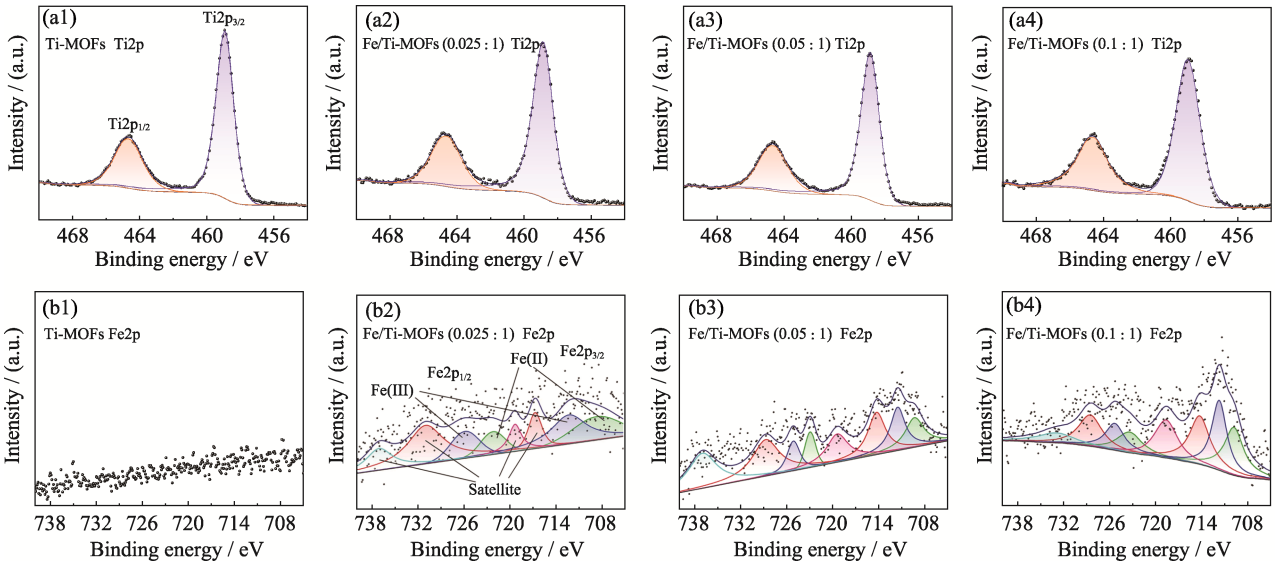

Fig. 2　High resolution XPS spectra of Ti2p (a1-a4) and Fe2p (b1-b4) of Ti-MOFs, Fe/Ti-MOFs (0.025 : 1), Fe/Ti-MOFs (0.05 : 1), and Fe/Ti-MOFs (0.1 : 1)

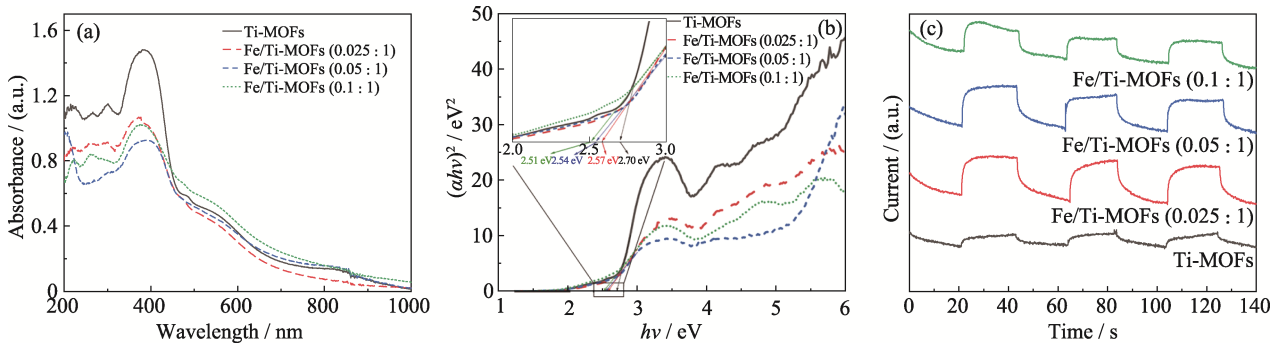

Fig. 3　UV-Vis spectra (a), bandgap fitting (b), and photoelectric response (c) of Ti-MOFs, Fe/Ti-MOFs (0.025 : 1), Fe/Ti-MOFs (0.05 : 1), and Fe/Ti-MOFs (0.1 : 1)

stability in aqueous environments increases with the increase of Fe doping level.

Subsequently, the electrochemical photocurrents of Fe/Ti-MOFs were investigated. As shown in Fig. 3(c), Fe/Ti-MOFs samples exhibited a photoelectric response. However, the intensity began to decrease in Fe/Ti-MOFs (0.1 : 1), which may be attributed to the reduced crystallinity of the sample, leading to an increased recombination rate of photogenerated carriers. As illustrated in Fig. 4(a), compared with the control group, MOFs samples demonstrated the clearance of MB under ultrasound stimulation. With increasing Fe doping levels, the MB removal efficiency under ultrasound conditions initially increased and then decreased, which was speculated to be related to the narrowing of the bandgap width and the reduction in crystallinity. Among the samples, Fe/Ti-MOFs (0.025 : 1) exhibited the highest efficiency, achieving nearly 50% MB clearance within 5 min. Further testing revealed a positive correlation between the MB degradation efficiency and ultrasound intensity of Fe/Ti-MOFs (0.025 : 1)(Fig. 4(b)). The ESR results (Fig. 4(c)) showed that a characteristic and strong signal corresponding to the intensity ratio of 1 : 2 : 2 : 1 for DMPO–OH could be observed in samples after ultrasound treatment, and the intensity of Fe/Ti-MOFs (0.025 : 1) was stronger than other samples. This indicated successful generation of hydroxyl radicals and sonocatalytic ability of Fe/Ti-MOFs (0.025 : 1).

In general, the bandgap has been widely recognized as the primary determinant of sonosensitizer performance[22-23]. However, our investigation reveals that defect engineering and crystallinity critically govern the sonocatalytic efficiency. The electron transfer process in sonocatalysis involves two sequential steps. Firstly, the generation of electron-hole pairs is predominantly controlled by bandgap width. Secondly, charge carriers migrate to material surfaces for redox reactions with microenvironmental species, leading to the generation of ROS[24]. Moderate metal doping facilitates electron spillover, whereas excessive doping creates detrimental trap states that promote electron-hole recombination, thereby hindering surface redox reactions. This mechanism is

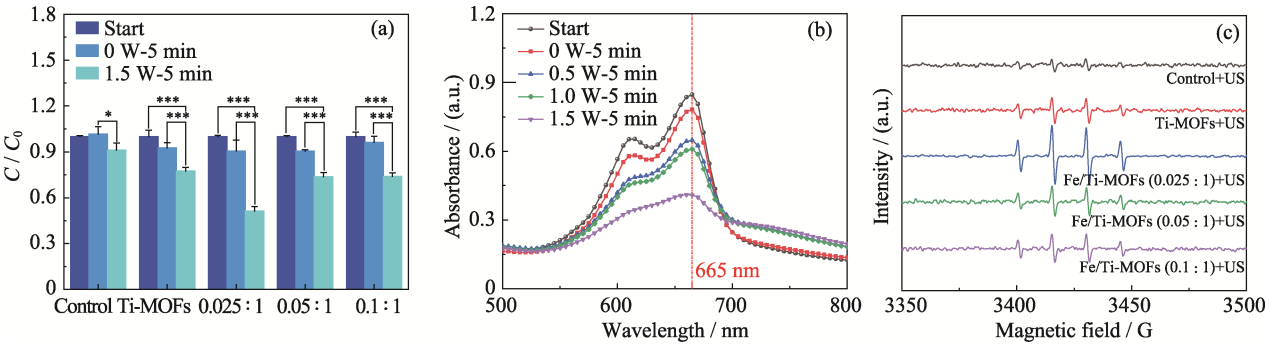

Fig. 4 MB degradation efficiencies of samples (a), absorption curves of Fe/Ti-MOFs (0.025 : 1) before and after ultrasound at different powers (b), and ESR spectra of samples under ultrasound (c)
Colorful figures are available on website

corroborated by the nonlinear relationship between Fe doping concentration and •OH generation efficiency, which initially increases and then declines as the doping level increases[17].

Moreover, our systematic investigation resolves the long-standing ambiguity concerning crystallinity effects: reduced crystallinity diminishes sonocatalytic efficiency by impairing acoustic induced electron transport. The findings establish a multiparameter design framework for sonosensitizers based on Ti-MOFs, emphasizing the synergistic optimization of bandgap engineering, precise doping control, and crystallinity regulation.

The bacterial culture results are shown in Fig. 5(a). For *E. coli*, under non-ultrasonic conditions, MOFs

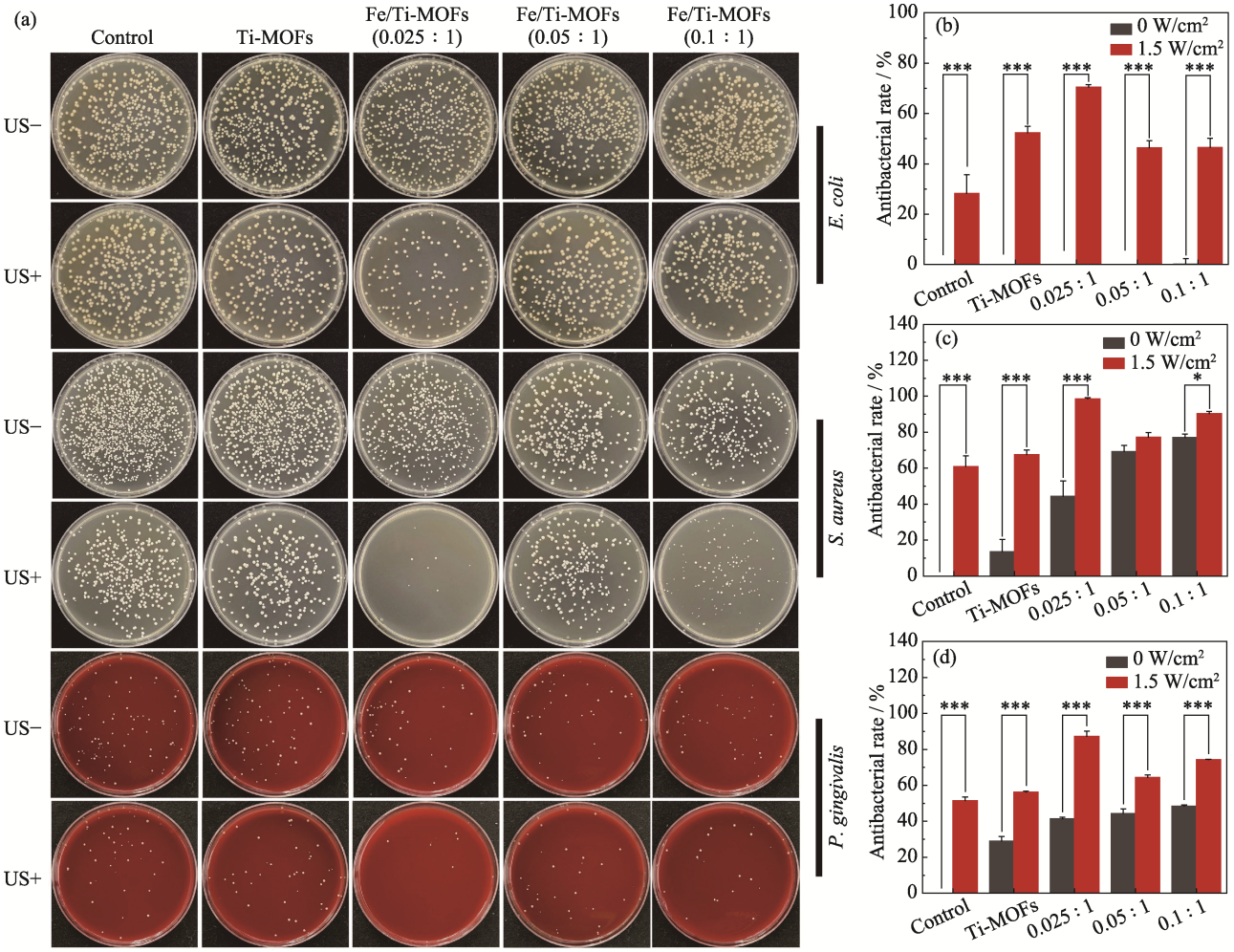

Fig. 5 Photos of re-cultivated bacterial colonies (a) and antibacterial rates against *E. coli* (b), *S. aureus* (c) and *P. gingivalis* (d) of Ti-MOFs, Fe/Ti-MOFs (0.025 : 1), Fe/Ti-MOFs (0.05 : 1), and Fe/Ti-MOFs (0.1 : 1) before and after ultrasonic treatment
US+ and US– represent under ultrasonic and non-ultrasonic conditions, respectively. Colorful figures are available on website

samples exhibited minimal antibacterial performance compared to the control group. Under ultrasound conditions, the number of bacterial colonies decreased in all groups, with the Fe/Ti-MOFs (0.025 : 1) group showing the most significant reduction, indicating superior antibacterial performance (Fig. 5(b)). For *S. aureus* and *P. gingivalis* under non-ultrasonic conditions, MOFs samples demonstrated antibacterial properties relative to the control group. The antibacterial efficacy was positively correlated with the Fe doping concentration. Under ultrasound conditions, the antibacterial rates of all groups increased, with the Fe/Ti MOFs (0.025 : 1) group exhibiting the most significant increase (Figs. 5(c, d)). It demonstrated that Fe/Ti-MOFs, especially Fe/Ti-MOFs (0.025 : 1), exhibited controllable antibacterial effects regulated by ultrasound stimulation, which was beneficial for achieving effective removal of bacterial pathogens.

The live-dead staining results are shown in Fig. 6(a) and cytotoxicity results are shown in Fig. 6(b). Compared with the control group, HGFs cultured with FM medium extracts of MOFs remained in an active state, with only a few cells exhibiting signs of death. Furthermore, HGFs showed good proliferative activity, suggesting that Fe/Ti-MOFs did not negatively affect cell proliferation. Samples with various doping ratios exhibited excellent biocompatibility. As shown in Figs. 6(c, d), the hemolysis rates detected from MOFs extracts cocultured with blood cells were all below 2% when compared with the positive control group, which falls within a safe range. It indicated that Ti-MOFs and Fe/Ti-MOFs samples possess good blood compatibility.

3 Conclusions

In summary, Fe doped Ti-MOFs were successfully synthesized with ultrasound responsiveness. The incorporation of heterogeneous Fe atoms alters the microstructure, lattice composition and band structure, narrowing the bandgap width and enabling them to generate ROS under ultrasound stimulation for effective eradication of bacteria and pathogens. Moreover, under non-ultrasound conditions, Fe/Ti-MOFs exhibit excellent biocompatibility and have no adverse effects on tissue repair processes, making them a promising candidate for periodontitis treatment.

Supporting Materials

Supporting materials related to this article can be found at https://doi.org/10.15541/jim20250165.

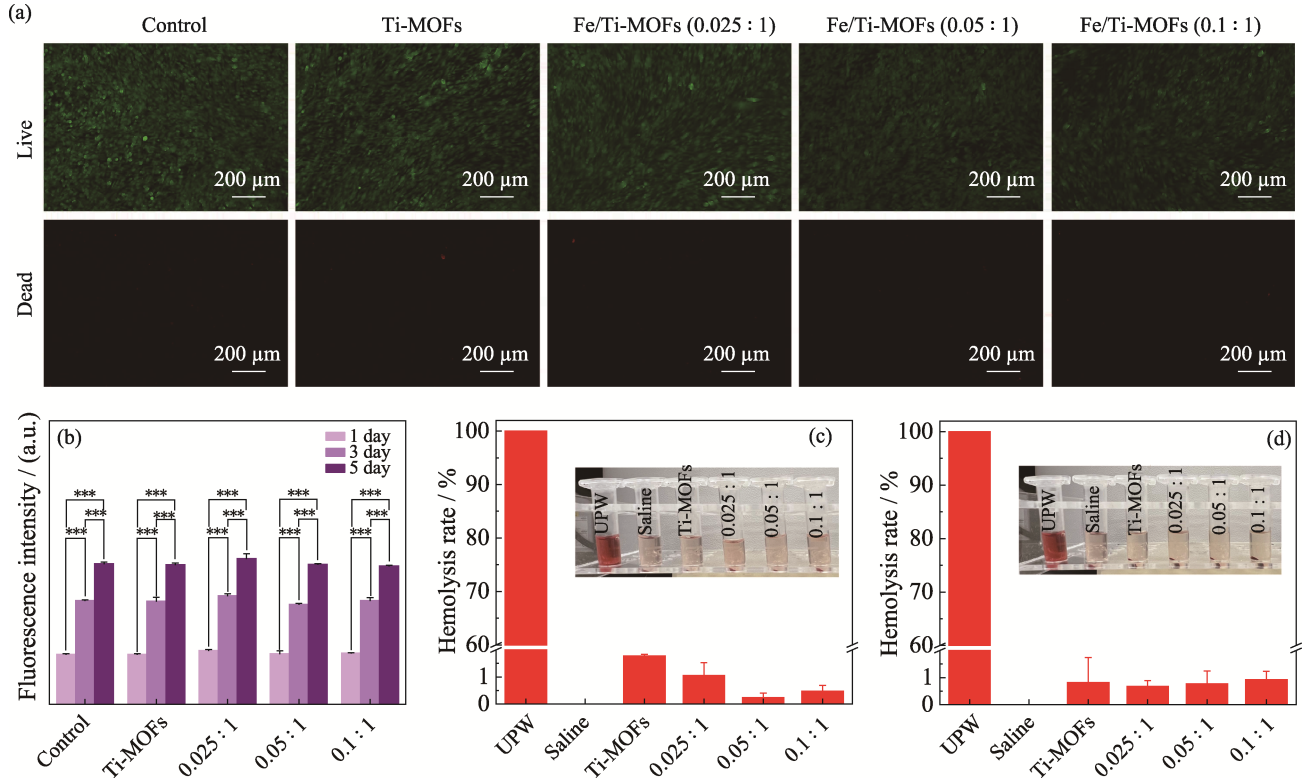

Fig. 6　Live-dead staining images (a), cell proliferation (b), and hemolysis tests (c, d) of Ti-MOFs, Fe/Ti-MOFs (0.025 : 1), Fe/Ti-MOFs (0.05 : 1), and Fe/Ti-MOFs (0.1 : 1)
Colorful figures are available on website

References:

[1] TAN X, LIU S, HU X, *et al*. Near-infrared-enhanced dual enzyme-mimicking Ag–TiO_{2-x}@alginate microspheres with antibactericidal and oxygeneration abilities to treat periodontitis. *ACS Applied Materials and Interfaces*, 2023, **15(1):** 391.

[2] MIYAUCHI S, KAWADA-MATSUO M, FURUSHO H, *et al*. Atrial translocation of *Porphyromonas gingivalis* exacerbates atrial fibrosis and atrial fibrillation. *Circulation*, 2025, **151(21):** 1527.

[3] LIU H, NAN Z, ZHAO C, *et al*. Emerging synergistic strategies for enhanced antibacterial sonodynamic therapy: advances and prospects. *Ultrasonics Sonochemistry*, 2025, **116:** 107288.

[4] ZHANG K, WANG T, HUANG X, *et al*. Ultrasound-mediated nanomaterials for the treatment of inflammatory diseases. *Ultrasonics Sonochemistry*, 2025, **114:** 107270.

[5] LI K, XU W, CHEN Y, *et al*. Piezoelectric nanostructured surface for ultrasound-driven immunoregulation to rescue titanium implant infection. *Advanced Functional Materials*, 2023, **33(28):** 2214522.

[6] CHEN H, LIU L, MA A, *et al*. Noninvasively immunogenic sonodynamic therapy with manganese protoporphyrin liposomes against triple-negative breast cancer. *Biomaterials*, 2021, **269:** 120639.

[7] PAN X, WU N, TIAN S, *et al*. Inhalable MOF-derived nanoparticles for sonodynamic therapy of bacterial pneumonia. *Advanced Functional Materials*, 2022, **32(25):** 2112145.

[8] QIN W, YANG Q, ZHU C, *et al*. A Distinctive insight into inorganic sonosensitizers: design principles and applicationdo-mains. *Small*, 2024, **20(25):** 2311228.

[9] LI D, YANG Y, LI D, *et al*. Organic sonosensitizers for sonodynamic therapy: from small molecules and nanoparticles toward clinical development. *Small*, 2021, **17(42):** 2101976.

[10] YANG F, DONG J, LI Z, *et al*. Metal–organic frameworks (MOF)-assisted sonodynamic therapy in anticancer applications. *ACS Nano*, 2023, **17(5):** 4102.

[11] DAN-HARDI M, SERRE C, FROT T, *et al*. A new photoactive crystalline highly porous titanium(IV) dicarboxylate. *Journal of the American Chemical Society*, 2009, **131(31):** 10857.

[12] VERMOORTELE F, MAES M, MOGHADAM P Z, *et al*. *p*-xylene-selective metal–organic frameworks: a case of topology-directed selectivity. *Journal of the American Chemical Society*, 2011, **133(46):** 18526.

[13] NGUYEN H L. Perspectives on titanium-based metal–organic frameworks. *Journal of Physics: Energy*, 2021, **3(2):** 021003.

[14] CHEN J, CHENG F, LUO D, *et al*. Recent advances in Ti-based MOFs in biomedical applications. *Dalton Transactions*, 2022, **51(39):** 14817.

[15] LIANG S, XIAO X, BAI L, *et al*. Conferring Ti-based MOFs with defects for enhanced sonodynamic cancer therapy. *Advanced Materials*, 2021, **33(18):** 2100333.

[16] WANG Q, TIAN Y, YAO M, *et al*. Bimetallic organic frameworks of high piezovoltage for sono-piezo dynamic therapy. *Advanced Materials*, 2023, **35(41):** 2301784.

[17] LI Y, REN Z, HE Z, *et al*. Crystallinity-defect matching relationship of g-C_3N_4: experimental and theoretical perspectives. *Green Energy and Environment*, 2024, **9(4):** 623.

[18] JIN Y, LIU F, LI Y, *et al*. Efficient adsorption of azo anionic dye Congo Red by micro-nano metal-organic framework MIL-68(Fe) and MIL-68(Fe)/chitosan composite sponge: preparation, characterization and adsorption performance. *International Journal of Biological Macromolecules*, 2023, **252:** 126198.

[19] WANG Y, FENG W, LI J, *et al*. A novel route for the facile synthesis of NH_2-MIL-53(Fe) and its highly efficient and selective adsorption of Congo Red. *Inorganica Chimica Acta*, 2023, **547:** 121332.

[20] OLCZAK T, SIMPSON W, LIU X, *et al*. Iron and heme utilization in *Porphyromonas gingivalis*. *FEMS Microbiology Reviews*, 2005, **29(1):** 119.

[21] WÓJTOWICZ H, GUEVARA T, TALLANT C, *et al*. Unique structure and stability of HmuY, a novel heme-binding protein of *Porphyromonas gingivalis*. *PLOS Pathogens*, 2009, **5(5):** e1000419.

[22] WANG X, ZHONG X, BAI L, *et al*. Ultrafine titanium monoxide (TiO_{1+x}) nanorods for enhanced sonodynamic therapy. *Journal of the American Chemical Society*, 2020, **142(14):** 6527.

[23] ZHANG D Y, LIU H, YOUNIS M R, *et al*. *In-situ* TiO_{2-x} decoration of titanium carbide MXene for photo/sono-responsive antitumor theranostics. *Journal of Nanobiotechnology*, 2022, **20(1):** 53.

[24] GUAN S, XU W, TAN J, *et al*. Metainterface heterostructure enhances sonodynamic therapy for disrupting secondary biofilms. *ACS Nano*, 2024, **18(23):** 15114.

Fe 掺杂 Ti-MOFs 用于牙周炎抗菌声动力治疗

王浩宇[1,2], 柯　学[1,2], 关世伟[1,2], 钱　仕[1,2], 刘宣勇[1,2]

(1. 中国科学院 上海硅酸盐研究所, 关键陶瓷材料全国重点实验室, 上海 200050; 2. 中国科学院大学 材料与光电研究中心, 北京 100049)

摘　要: 牙周炎是临床极富挑战的问题, 由口腔致病菌过度生长失衡引起, 可导致牙周组织的不可逆损伤。与清创术相比, 抗菌声动力疗法(aSDT)具有优异的生物相容性和组织穿透能力, 是一种有前景的替代方案。本工作制备了铁掺杂的钛基金属有机框架(Fe/Ti-MOFs), 研究了铁掺杂与声催化效率间的量效关系。引入 Fe 能够调节 MOFs 的能带结构和结晶度, 且未改变其晶格结构。结果表明, Fe/Ti-MOFs 在超声作用下表现出增强的羟基自由基(•OH)产生能力, 从而催化杀灭细菌病原体。其中, Fe/Ti 摩尔比为 0.025 : 1 的样品表现出较佳的声催化性能, 且受带隙工程、铁掺杂浓度和结晶度的共同调节。此外, 牙龈成纤维细胞增殖和活死染色结果表明, Fe/Ti-MOFs 具有优异的生物相容性。超声响应的 Fe/Ti-MOFs 材料为牙周炎的 aSDT 提供了新的见解和策略, 有望避免抗生素的不良反应。

关　键　词: 抗菌; 声动力治疗; 牙周炎; 金属有机框架; NH_2-MIL-125(Ti)

中图分类号: R781　　**文献标志码:** A　　**文章编号:** 1000-324X(2026)04-0527-09

Supporting Materials:

Fe Doped Ti-MOFs for Enhanced Antibacterial Sonodynamic Therapy of Periodontitis

WANG Haoyu[1,2], KE Xue[1,2], GUAN Shiwei[1,2], QIAN Shi[1,2], LIU Xuanyong[1,2]

(1. State Key Laboratory of High Performance Ceramics, Shanghai Institute of Ceramics, Chinese Academy of Sciences, Shanghai 200050, China; 2. Center of Materials Science and Optoelectronics Engineering, University of Chinese Academy of Sciences, Beijing 100049, China)

S1 Synthesis of Fe/Ti-MOF-ITO conductive glass composite electrodes

Ti-MOFs and bimetallic Fe/Ti-MOFs were dispersed in ultrapure water to prepare a dispersion solution of 5.0 mg/mL, which was uniformly dispersed by ultrasound. Afterwards, 40 μL of dispersed liquid droplets was added to the surface of ITO conductive glass (1 cm^2) and baked at 100 ℃. After the moisture was completely removed, the MOF-ITO composite electrode was obtained.

Table S1 Raw material usage in preparation process of Fe/Ti-MOFs with different Fe : Ti ratios

Sample	$H_2BDC\text{-}NH_2$/g	$Fe(acac)_3$/mg	TTIP/mL	DMF/mL	CH_3OH/mL
Ti-MOFs	2.72	0	1.15	45.0	5.00
Fe/Ti-MOFs (0.025 : 1)	2.72	33.1	1.15	45.0	5.00
Fe/Ti-MOFs (0.05 : 1)	2.72	66.1	1.15	45.0	5.00
Fe/Ti-MOFs (0.1 : 1)	2.72	132.2	1.15	45.0	5.00

Table S2 Diffraction peak parameters of different crystal planes of Ti-MOFs and different Fe/Ti-MOFs materials

Sample		Ti-MOFs	Fe/Ti-MOFs (0.025 : 1)	Fe/Ti-MOFs (0.05 : 1)	Fe/Ti-MOFs (0.1 : 1)
(101)	Intensity	1858	1405	1123	546
	FWHM/°	0.196	0.192	0.238	0.317
(100)	Intensity	483	386	382	205
	FWHM/°	0.160	0.147	0.164	0.174
(001)	Intensity	1885	1340	1093	631
	FWHM/°	0.208	0.215	0.303	0.543
(211)	Intensity	2171	1612	1427	865
	FWHM/°	0.180	0.170	0.207	0.362

Table S3 Specific surface area and pore volume data of Ti-MOFs and different Fe/Ti-MOFs

Sample	S_{BET}/($m^2 \cdot g^{-1}$)	S_{DFT}/($m^2 \cdot g^{-1}$)	V_{pore}/($cm^3 \cdot g^{-1}$)
Ti-MOFs	1132.08	1722.72	0.69
Fe/Ti-MOFs (0.025 : 1)	1134.90	1702.66	0.66
Fe/Ti-MOFs (0.05 : 1)	1175.66	1736.29	0.74
Fe/Ti-MOFs (0.1 : 1)	1033.73	1533.40	0.77

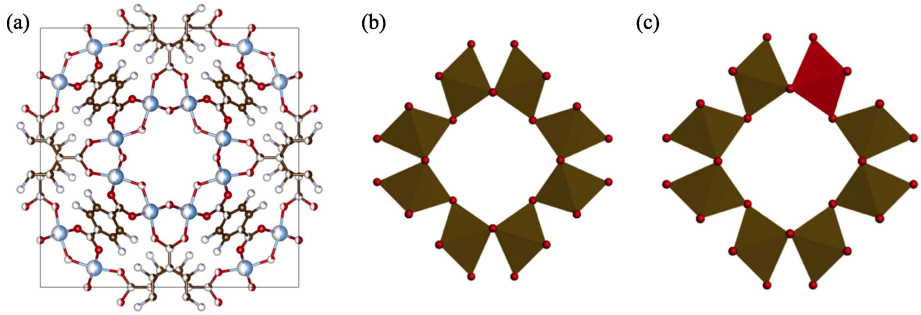

Fig. S1 (001) crystal plane of NH_2-MIL-125(Ti) (a) and secondary building units before (b) and after (c) Fe doping

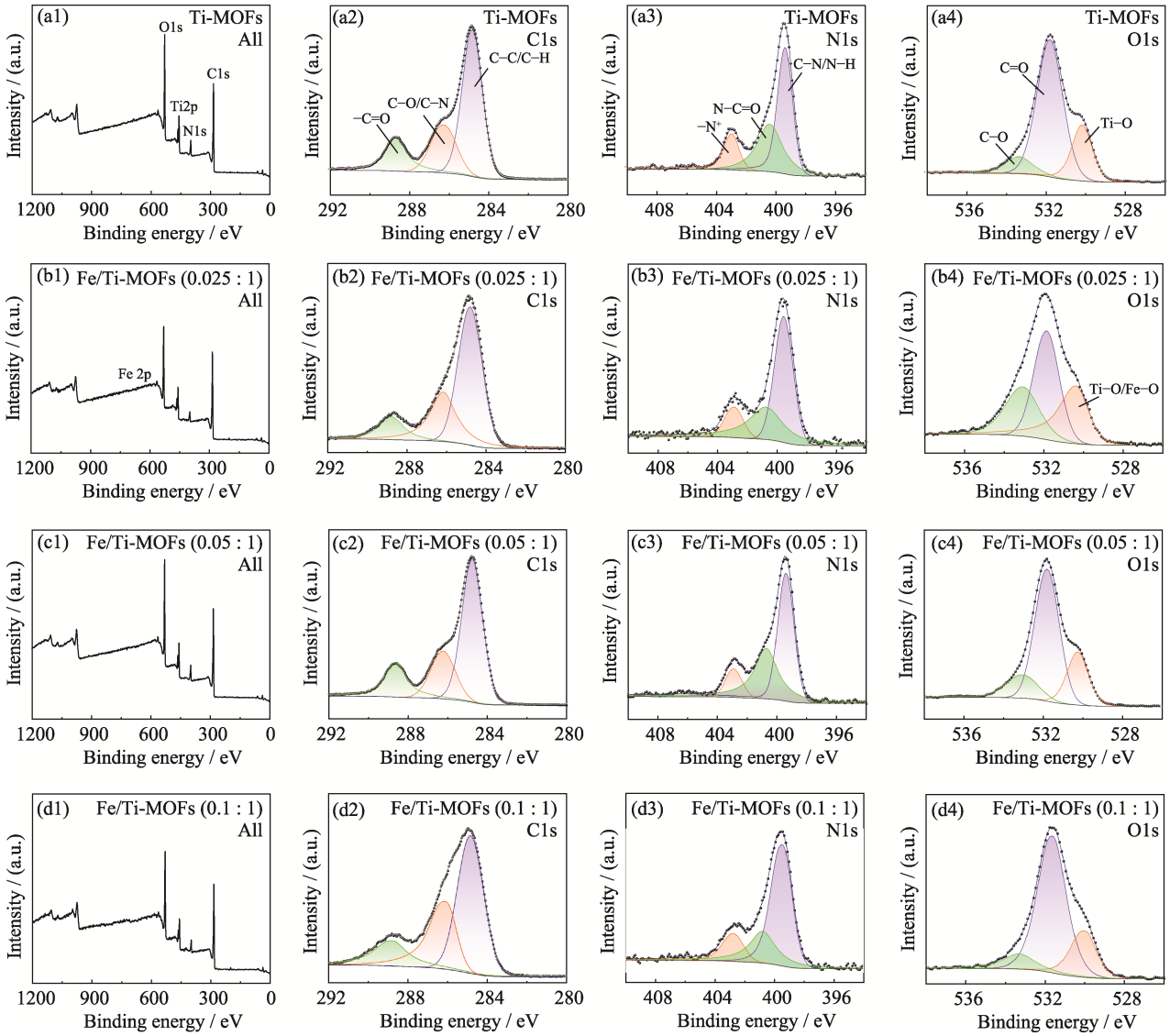

Fig. S2　Full XPS spectra (a1-d1) and high-resolution C1s (a2-d2), N1s (a3-d3), and O1s (a4-d4) XPS spectra of Ti-MOFs, Fe/Ti-MOFs (0.025 : 1), Fe/Ti-MOFs (0.05 : 1), and Fe/Ti-MOFs (0.1 : 1)

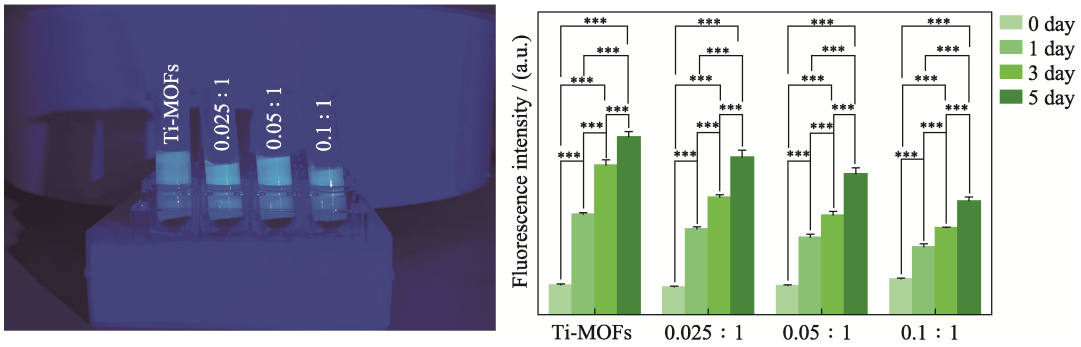

Fig. S3　Degradability evaluation of Ti-MOFs, Fe/Ti-MOFs (0.025 : 1), Fe/Ti-MOFs (0.05 : 1), and Fe/Ti-MOFs (0.1 : 1)